machines

MDPI

*Article*

# Open On-Limb Robot Locomotion Mechanism with Spherical Rollers and Diameter Adaptation

**Luz M. Tobar-Subía-Contento [1,2,*], Anthony Mandow [2] and Jesús M. Gómez-de-Gabriel [2]**

[1] Facultad de Ingeniería en Ciencias Aplicadas, Universidad Técnica del Norte, Ibarra 100150, Ecuador
[2] Institute for Mechatronics Engineering and Cyber-Physical Systems (IMECH.UMA), Universidad de Málaga, 29071 Málaga, Spain; amandow@uma.es (A.M.); jesus.gomez@uma.es (J.M.G.-d.-G.)
* Correspondence: lmtobarsubia@utn.edu.ec

**Abstract:** The rapid development of wearable technologies is increasing research interest in on-body robotics, where relocatable robots can serve as haptic interfaces, support healthcare measurements, or assist with daily activities. However, on-body mobile robotics poses challenges in aspects such as stable locomotion and control. This article proposes a novel small robot design for moving on human limbs that consists of an open grasping mechanism with a spring linkage, where one side holds a pivoting differential drive base (PDDB) with two spherical rollers, and the other side holds an actuated roller for grasping and stabilization. The spherical rollers maintain contact at three points on the limb, optimizing stability with a minimal number of rollers and integrating DC motors within. The PDDB wheels (spherical rollers) enable directional changes on limb surfaces. The combination of the open mechanism, the PDDB, and the spherical rollers allows adaptability to diameter variations along the limb. Furthermore, the mechanism can be easily put on or removed at any point along the limb, eliminating the need to slip the robot over the hand or foot. The kinematic model for the proposed mechanism has been developed. A cascade control strategy is proposed with an outer loop for stable grasping and an inner loop for trajectory adjustments using PDDB roller velocities. An on-limb robot prototype has been built to test its applicability to human arms. Simulation and experimental results validate the design.

**Keywords:** on-body mobile robot; physical human–robotic interaction; spherical rollers; grasping; limb-climbing robot



**Citation:** Tobar-Subía-Contento, L.M.; Mandow, A.; Gómez-de-Gabriel, J.M. Open On-Limb Robot Locomotion Mechanism with Spherical Rollers and Diameter Adaptation. *Machines* **2024**, *12*, 455. https://doi.org/10.3390/machines12070455

Academic Editor: Dan Zhang

Received: 31 May 2024
Revised: 26 June 2024
Accepted: 2 July 2024
Published: 4 July 2024



## 1. Introduction

The rapid advancement of new technologies has sparked the development and significant commercial impact of wearable smart devices that can be attached to the body to improve quality of life through safety, assistance, and entertainment [1–3]. The concept of wearable robotics as person-oriented systems was coined over a decade ago to primarily refer to exoskeletons, orthotic robots, and prosthetic robots [4,5]. However, the growing interest in lightweight and compact devices has broadened the notion of robot wearability to include miniature robots that can either be affixed to the body [6–9] or move along its surface. In this sense, dynamic wearable technology [10], where small robots can move on or around the human body, can extend the capabilities of wearable smart devices in applications such as healthcare measurements [11,12], haptic interfaces [13,14], fashion expression [15], and support and assistance with activities of daily living (ADL) [16,17].

Nevertheless, on-body mobile robotics is a challenging topic that requires specific research in key technological aspects such as adhesion, locomotion design, and control.

Generally, climbing robots for industrial and maintenance applications have adopted various adhesion mechanisms such as vacuum suction cups, grippers, magnetic systems, or bioinspired methods mimicking geckos or insects [18–20]. Even if the requirements for wearable robots differ significantly from industrial solutions [21], some studies have

proposed locomotion designs that adapt some of these mechanisms to on-body robots. For instance, SkinBot [11,21] has an inch-worm locomotion system that employs two legs with suction cups to navigate on human skin and collect biosignals, yet vacuum pumps pose a challenge for achieving untethered devices. Furthermore, some works have investigated cloth climbing mechanisms that could be used for on-body robots. Thus, gripper-based locomotion can be employed to grasp fabric, taking advantage of the soft and deformable characteristics of loose clothing. Clothbot [12] employs a gripper consisting of a passive spring and two tangential differential drive wheels, allowing it to roll along the fold within the gripper. Given that movement direction is restricted by the fold, an articulated tail can use gravity to assist steering [22]. In Rubbot [23], a passive folder frame holds two grippers for differential motion. Moreover, Rovables [24] are differential drive miniature robots that use magnetic attraction between wheels and a rod that moves on the fabric's inner side. Additionally, gecko-inspired adhesion was used for the feet of the CLASH lightweight micro-hexapod to climb on loose clothing [25]. In general, cloth-climbing robots allow for navigation on any part of the body where clothing is smooth. However, they are not suitable for applications requiring direct contact with the body, such as healthcare measurements. Moreover, their design primarily focuses on managing folds and other interactions with flexible fabric, which limits maneuverability. Alternative locomotion designs have avoided adhesion issues by employing smooth rails or tracks affixed to the clothing worn by the user [26]. The rail locomotion design of the Calico robot [14] relies on wheels, a rail attachment system, and a track-switching mechanism for bifurcations.

In contrast, on-limb mobile robots designed to move along the wearer's arm [13,16,17,27] are based on locomotion systems that make direct contact with the limb, either on bare skin or through tight clothing. These on-limb mobile robot designs prioritize a snug fit by exerting gentle pressure against the limb, relying less on adhesion, and using surface materials and textures that favor both grip and comfort. Additionally, on-limb robots require adaptability to the varying diameters of the limb (e.g., from the wrist to the upper arm). On-limb mobile robots are related to out-of-pipe climbing robots in industrial applications [28,29]. Some pipe climbing robots [30,31] have addressed diameter variation with adaptable clamping mechanisms that can be mechanically adjusted to different pipe sizes before use, but are not designed for pipes with diameter variations along their length. In general, the designs and construction of industrial solutions are mostly unsuitable for human limbs due to their heavy and complex structures [31,32], even if current research in soft robots [33,34] aims at lighter and compliant pipe crawling mechanisms that could be suitable for human–robot interaction [35]. In this sense, Knitskin [27] is a textile sleeve-like robot designed for moving along the user's forearm that needs a compressor for pressurizing pneumatic actuators. Nevertheless, most methods for on-limb motion rely on rigid locomotion with self-actuated electric servo-motors. Thus, the Movelet robot for positional haptic feedback [13] consists of a closed bracelet with four evenly distributed wheels connected by pairs of spring suspensions, allowing for small diameter adjustments along the forearm. The wearable bracelet robot proposed by Kimura et al. [16] is based on rolling spherical capsules with internal motors, linked by alternating rigid links and a flexible rubber band with an actuated reel for diameter adaptation. Alternatively, the bathing assistance robot proposed by Liu et al. [17] is a four-wheel mechanism designed for single-track locomotion along the user's arm, pulling a cleaning fabric sleeve that also serves to hold the robot in place. All of these mechanisms depend on closed bracelets or sleeves that must be slid over the wearer's hand, which limits applicability in situations where active user involvement or human assistance is challenging or unexpected, such as remote health monitoring for patients or victims.

In this work, we propose an open mechanism for on-limb locomotion that can be put on or removed at any point of the limb without slipping the robot over the hand or foot. This novel locomotion design has a minimum number of wheels: two actuated spherical rollers for differential drive and another actuated spherical roller for grasping and stabilization. A triangular configuration provides stability (i.e., three points of contact

provide a stable support base for an object) and can accommodate uneven surfaces. Some studies [36,37] have demonstrated that using three fingers on robotic grippers improves the capability to grasp more complex irregular objects. In particular, spherical rollers [38] have been employed as fingertips for in-hand manipulation [36], facilitating the manipulation and reorientation of objects with different shapes and enabling continuous rotation and adaptability to changes in the contact state.

In particular, the major contributions of this article are as follows:

1. A new robot designed to move on human limbs featuring an open grasping mechanism with a spring linkage. One side has a pivoting differential drive base (PDDB) with two actuated spherical rollers, and the other side has an actuated roller for grasping and stabilization.
2. The kinematic analysis of the proposed robot configuration estimates the circumcenter coordinate, the current limb radius, and the actual roller contact points from the joint angle measurements. These values are necessary for estimating the actual differential drive wheel distance for motion control.
3. A cascade control system, combined with the passive spring linkage, allows for adaptation to varying limb diameters. The outer loop ensures stable grasping, while the inner loop adjusts the trajectory using PDDB roller velocities. A Lyapunov stability analysis is also provided.

Additionally, the article presents experimental results from both simulations and a real on-arm prototype. To our knowledge, this is the first analysis of a locomotion system based on spherical rollers with proprioceptive estimation of limb diameter changes.

The rest of this paper is organized as follows. Section 2 presents the proposed design. Section 3 offers a kinematic analysis locomotion system. The cascade control system is described in Section 4. Section 5 discusses the experimental results. Finally, Section 6 summarizes the key findings and offers conclusions.

## 2. On-Limb Mobile Robot Design

This section offers an overview of the proposed design and describes the grasping model, highlighting the concept of central alignment for ensuring stability while moving on the limb.

### *2.1. Design Overview*

The concept and main elements of the proposed robot design are illustrated in Figure 1. The system consists of an open symmetrical two-link mechanism with a passive spring joint, where the first link holds a differential drive base with a passive pivot joint. The pivoting differential drive base (PDDB) has two active spherical rollers that move along the limb. The spring joint presses the PDDB over the limb, ensuring the rollers are always in contact with it. The centerline of the PDDB is connected to Link 1 using a free pivot joint aligned with the motion axis corresponding to the measured articulation variable $\theta_1$. Moreover, Link 1 and Link 2 are connected by a passive spring joint (measured articulation variable $\theta_2$) to facilitate grasping and adaptation to changes in limb diameter. The synergy between the pivot and spring joints enables stable and adaptable locomotion along the limb. The second link has a fixed (i.e., non-articulated) platform holding a 1 DoF spherical roller that provides the grasping point. Furthermore, this wheel is active to maintain an aligned robot pose relative to the limb.

The rotation axes of the three rollers (i.e., two spherical wheels in a differential drive configuration plus an opposing grasping wheel) are in the same plane. Spherical rollers allow for stable grasps independent of its orientation [36] and limb radii. Also, the spherical design of the rollers allows them to have individual DC motors inside, with encoders for velocity control, reducing hardware size and utilizing internal volume [36]. The PDDB rollers are used to change the heading. At the same time, the actuator of the third one provides a grasping effect, holding the device on the limb with a velocity equivalent to the PDDB's linear velocity. These rollers are suitable for curved surfaces, providing a single

contact point regardless of surface curvature. Moreover, the combination of the spring joint, the free-pivoting mechanism, and the spherical rollers allows continuous 3-wheel contact with the limb surface. PDDB wheels can be used to correct the orientation of the trajectory, preventing the deterioration of the stable grasp during locomotion.

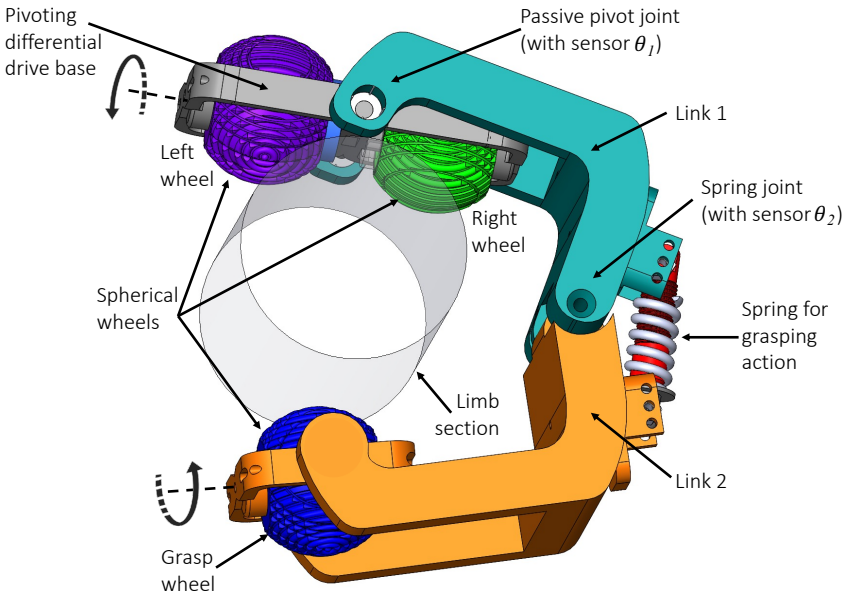


**Figure 1.** Illustration of the concept and main elements of the on-limb mobile robot. Colors indicate the different parts of the locomotion system: two links with a spring joint, the pivoting differential drive base, and three actuated 1 DOF spherical rollers.

All in all, the proposed design enables adaptability to variations in the limb section: the passive spring provides continuous adaptation to size changes, the PDDB ensures contact and allows for differential drive heading corrections against shape variations, and the continuous curvature of spherical rollers provides smooth motion independent of the actual contact points. Additionally, the mechanism can be easily attached or removed at any point on the limb without requiring the robot to be slipped over the hand or foot.

### *2.2. Grasp Model*

Figure 2 shows a cross-sectional diagram of the proposed robot configuration on a cylindrical limb. The robot can be considered planar, with all roller axles in the same plane, and the axles of the spring and pivot joints are perpendicular to this plane. In this work, point coordinates in the local robot frame $XYZ$ are denoted by subindexes $x$, $y$, and $z$ (e.g., $P = P_x, P_y, P_z$). In particular, $XYZ$ is placed at the center of the PDDB, where the $Z$-axis coincides with the pivot axis, and the $X$-axis coincides with the rotation axle of the differential drive wheels. Hence, the pivot joint point is $P_1 = (0, 0, 0)$. For the kinematic chain, we have followed a Denavit–Hartenberg convention. The origin of the $x_1y_1z_1$ frame for Link 1, which holds the PDDB, coincides with that of the robot's frame, with the $z_1$-axis aligned with $Z$. Link 1 has a length $L_1$ and rotates around the $Z$-axis with a pivot joint angle $\theta_1$ measured relative to the $X$-axis.

The local frame for Link 2, which has a length $L_2$, originates at the spring joint point $P_2$ and rotates around the $z_2$-axis, with the $x_2$-axis aligned with the link segment $\overline{P_2G}$. The spring joint angle $\theta_2$ is defined between $x_1$ and $x_2$. The joint vector is defined as $\boldsymbol{\theta} = [\theta_1, \theta_2]^T$.

The frames for the left, right, and grasping spherical rollers (i.e., $x_Ly_Lz_L$, $x_Ry_Rz_R$, and $x_Gy_Gz_G$) are placed at the respective centers $L$, $R$, and $G$, with rotation around the corresponding $x$-axis. The Cartesian coordinates for the grasp roller center $G$ are computed from $P_2$ and the spring-joint angle $\theta_2$. The contact points relevant for grasp stability and motion control are denoted as $P_l$, $P_r$, and $P_g$ for the left, right, and grasp rollers, respectively.

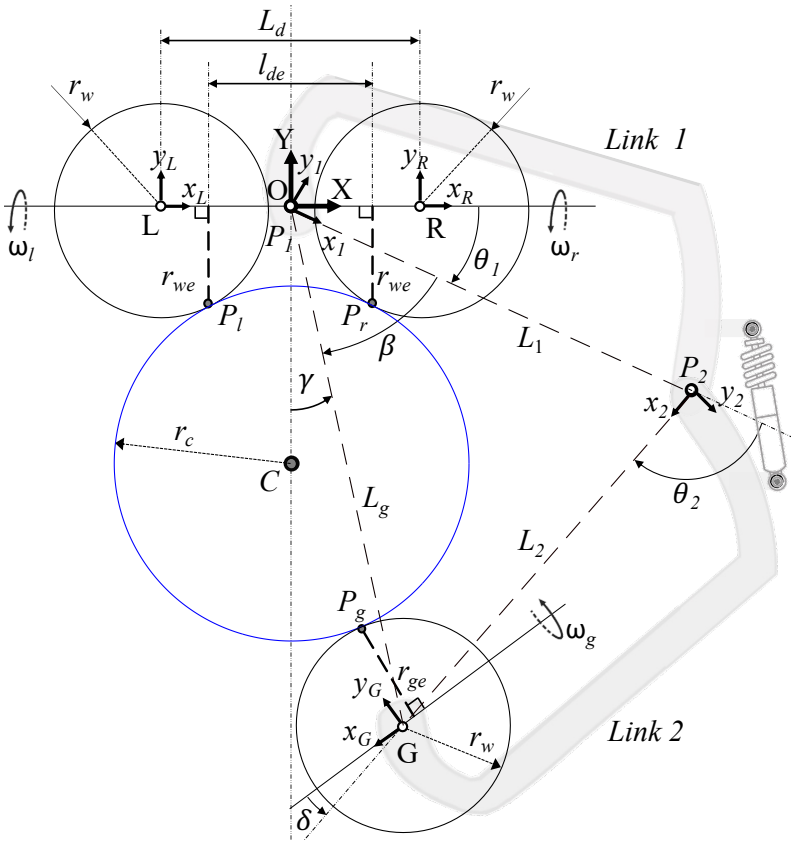


**Figure 2.** Cross-sectional schematic diagram of the on-limb mobile robot mechanism. The cylindrical limb is depicted in blue.

The locomotion of the PDDB along the limb's longitudinal axis is illustrated in Figure 3, which shows a top view of the robot. This locomotion is characterized by independently controlled wheels (left and right) working in tandem to maintain a straight-line trajectory. The vehicle heading is parallel to the longitudinal limb axis in the centered orientation, meaning the pivot point is in the center. An off-centered state occurs when the robot deviates from the longitudinal axis. Moreover, orientation error $\alpha$ affects the cylindrical section shape, which becomes elliptical. The PDDB's linear velocity is denoted as $V$, while the right and left wheels' linear velocities are $v_l$ and $v_r$, respectively.

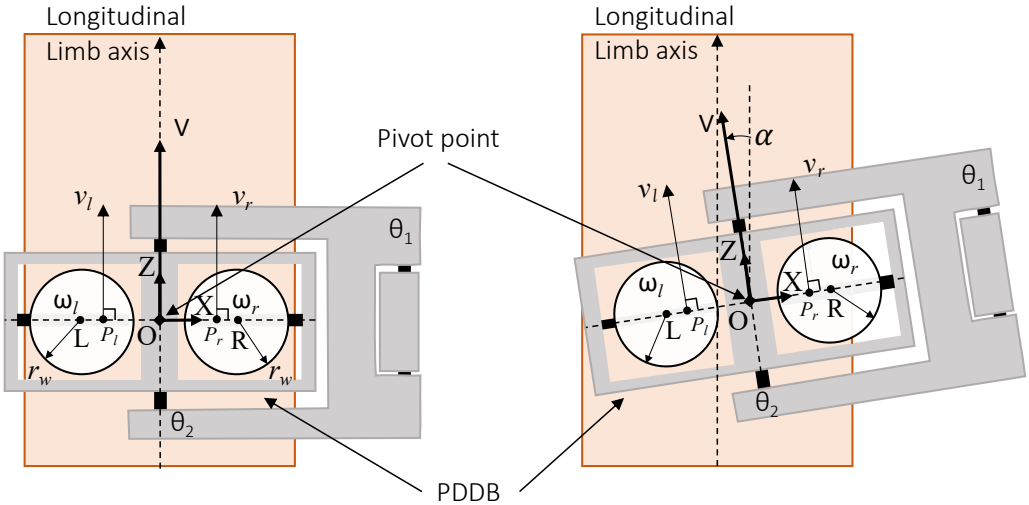


**Figure 3.** Top view of the on-limb mobile robot with respect to the limb's longitudinal axis: centered (**left**) and uncentered (**right**).

### 2.3. Stability of Grasp and Alignment Error

When considering grasp with $d$ fingers under a planar friction-less grasp, a stable equilibrium grasp $B(q)$ is achieved when the total wrench $W(q)$ due to the finger forces $F_i, i = 1 \ldots d$ is zero. In the case of the proposed circular geometry, with no frictions, the forces are pure normal forces with respect to the center of the grasped body (i.e., $F_i = \eta_i$). The condition for the equilibrium grasp [39] for a three finger (i.e., $d = 3$) friction-less grasping is that $W(q) = 0$ with $W(q) = \sum_{i=1}^{d} \lambda_i \eta_i(q)$ and $\lambda_i \geq 0$ (i.e., positive $\lambda_i$ coefficients can be found).

In this case, the planar grasping configurations that make possible a null wrench $W(q) = 0$ are illustrated in Figure 4. In Figure 4a, a null wrench is possible with non-negative $\lambda_i$. Figure 4b shows the limit case, where a positive value of $\eta_2$ makes a positive Wrench under the friction-less assumption. Finally, Figure 4c shows an unstable grasping configuration. Cases (b) and (c) occur also, respectively, for negative values of $\gamma$. Additionally, when considering surface frictions, the Coulomb friction replaces the normal forces with a friction cone [40], making the grasping area wider and providing a bigger, more practical, and stable grasp.

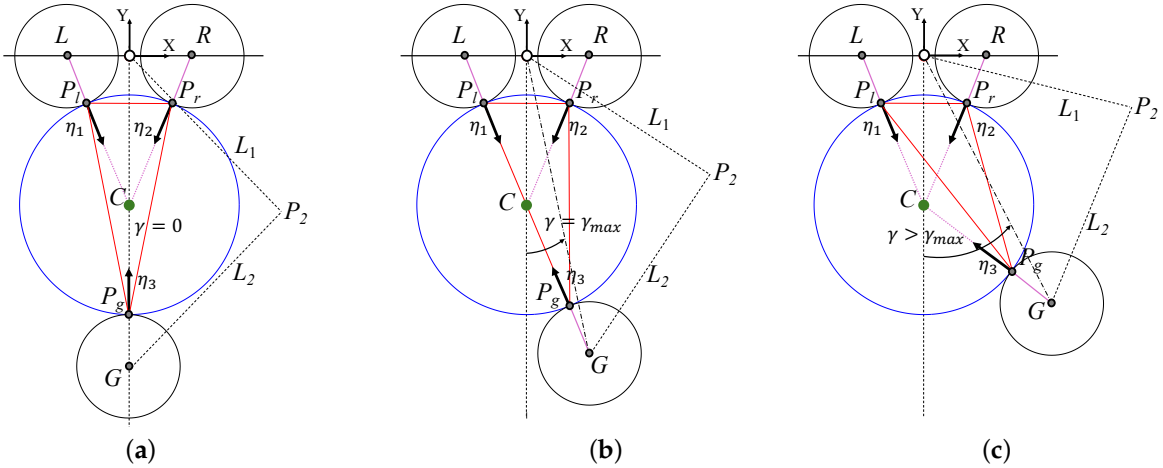


**Figure 4.** Illustration of grasp stability: (**a**) ideal central alignment ($\gamma = 0$), (**b**) maximum alignment error ($+\gamma_{max}$) for friction-less stable grasp, and (**c**) unstable grasp.

Graphically, in the desired robot grasping configuration (see Figure 4a), point $G$ lies on the $Y$ axis (i.e., $G_x = 0$) so the contact points $P_l$, $P_r$, and $P_g$ form an isosceles triangle whose circumcenter coincides with $C$. Additionally, the angle $\gamma$ of $\overline{OG}$ with respect to the $Y$ axis is null, indicating that the contact point triangle is centrally aligned with the limb section. Static grasping stability is maintained as long as $C$ remains within the contact point triangle. However, as the absolute value of $\gamma$ increases, the degree of central alignment decreases, potentially causing the robot to detach from the limb when $|\gamma| > \gamma_{\max}$. Specifically, $|\gamma_{\max}|$ is reached when $C$ lies on the segment $\overline{P_l P_g}$.

Therefore, the central alignment of the contact triangle and the limb section corresponds to maximum grasping stability, and $\gamma$ can be considered as the alignment error for controlling grasping stability. Alignment error $\gamma$ can be computed from the joint variable measurements $\theta_1$ and $\theta_2$, as well as the $L_1$ and $L_2$ lengths. First, the angle $\beta$ of $\overline{OG}$ with respect to $\overline{OP_2}$ is obtained using the law of sines:

$$\beta = \sin^{-1}\left(\frac{L_2 \cdot \sin(\pi - \theta_2)}{{L_1}^2 + {L_2}^2 - 2 \cdot L_1 \cdot L_2 \cdot \cos(\pi - \theta_2)}\right). \tag{1}$$

Then, $\gamma$ is given by:

$$\gamma = \frac{\pi}{2} - (\theta_1 + \beta). \tag{2}$$

## 3. Kinematics

This section describes the mathematical models of the robot kinematics. Figure 2 shows the schematic model, the coordinate systems, the joint variables, and the mechanism parameters. Tables 1 and 2 define the symbols of the major parameters and relevant variables used in the formulation, respectively. The simplifying assumptions for the kinematics analysis include considering the limb as a circular cylinder with a varying radius. The desired robot's locomotion is parallel to the cylinder's longitudinal axis. For this reason, the plane defined by the robot contact points is considered perpendicular to the longitudinal cylinder axis, resulting in a circular section. The analysis assumes pure rolling of rigid bodies without sliding and considers steering corrections sufficiently small to neglect the ellipsoidal components of the cylinder section.

**Table 1.** Design parameters.

| Parameter | Symbol |
|---|---|
| Roller radii | $r_w$ |
| Link length | $L_1$, $L_2$ |
| Distance between differential-drive wheel centers | $L_d$ |
| Angle between $L_2$ and $x_G$ axis | $\delta$ |

**Table 2.** Relevant variables.

| Variable Description | Symbol |
|---|---|
| Limb (cylinder) radius | $r_c$ |
| Effective left and right roller radii | $r_{we}$ |
| Effective grasping roller radius | $r_{ge}$ |
| Effective differential wheel distance (between differential-drive contact points) | $l_{de}$ |
| Roller contact points | $P_r$, $P_l$, $P_g$ |
| Circumcenter of the triangle defined by $\triangle LRG$ | $C$ |
| Length of the segment $\overline{OG}$ | $L_g$ |
| Angle between segment $L_1$ and $L_G$ | $\beta$ |
| Pivoting joint angle | $\theta_1$ |
| Spring joint angle | $\theta_2$ |
| Alignment error (Angle between segment $\overline{OG}$ and $Y$ axis) | $\gamma$ |

### *3.1. Limb Radii and Differential Wheel Distance Estimation*

We use the information from the joint angle measurements and the dimensions of the links to obtain the circumcenter coordinate $C = (C_x, C_y)$. To solve for $C_y$, we determine the equations for the bisectors of the triangle formed by the $\overline{LG}$, $\overline{LR}$, and $\overline{RG}$ segments, then we derive the midpoints of the $\overline{LG}$ segment, and finally we find the slope of its perpendicular line. Hence, $C_y$ is given by:

$$C_y = \frac{1}{2}\left((G_x + L_x)\frac{G_x - L_x}{G_y - L_y} + (G_y + L_y)\right). \tag{3}$$

Moreover, as the PDDB is symmetrical with respect to $Y$, then $C_x = 0$.

Then, the limb (i.e., cylinder) radius $r_c$ can be obtained by applying the Pythagorean theorem from a distance between $L$, $O$, and $C$ less the wheel radius $r_w$:

$$r_c = \sqrt{{C_y}^2 + {L_x}^2} - r_w. \tag{4}$$

As for the computation of contact points, the angle $\phi$ between $\overline{LC}$ and $X$ is given by $\phi = -\tan^{-1}(m_{LC})$, where $m_{LC}$ is the slope of $\overline{LC}$. Then, the coordinates $P_l = (P_{l_x}, P_{l_y})$ of the left roller contact points are:

$$P_l = \begin{bmatrix} P_{l_x} \\ P_{l_y} \end{bmatrix} = \begin{bmatrix} L_x + r_w \cdot \cos(\phi) \\ L_y + r_w \cdot \sin(\phi) \end{bmatrix}, \tag{5}$$

and $P_r$ is symmetrical with respect to $Z$:

$$P_r = \begin{bmatrix} P_{r_x} \\ P_{r_y} \end{bmatrix} = \begin{bmatrix} -P_{l_x} \\ P_{l_y} \end{bmatrix}. \tag{6}$$

Similarly, the coordinates of contact point $P_g = (P_{g_x}, P_{g_y})$ are:

$$P_g = \begin{bmatrix} P_{g_x} \\ P_{g_y} \end{bmatrix} = \begin{bmatrix} G_x - r_w \cdot \cos(\rho) \\ G_y - r_w \cdot \sin(\rho) \end{bmatrix}, \tag{7}$$

where $\rho$ is the angle between $\overline{GC}$ and $X$.

A spherical roller ensures a contact point when the robot moves on a non-planar surface. However, actual contact points $P_*$ do not lie on the corresponding rollers' $y_*$-axis (see Figure 2), so the constant distance $L_d$ between the PDDB wheels centers is not suitable for differential drive computations. Moreover, the contact points of spherical wheels change along the path due to variations in the cylinder's radius. Therefore, the distance between $P_{l_x}$ and $P_{r_x}$ is the effective differential drive wheel distance $l_{de}$, which can be obtained from Equation (5) as:

$$l_{de} = |2 \cdot P_{l_x}|. \tag{8}$$

Similarly, the effective wheel radius is defined as the perpendicular distance from the wheel rotation axis to the limb at the contact point, which is $r_{we}$ for the PDDB rollers and $r_{ge}$ for the grasp roller (see Figure 2). To determine $r_{we}$, we use the relationship defined by the right triangle formed by $L$, the roller radius $r_w$, and the difference of the roller distance $L_d - l_{de}$. Applying the Pythagorean theorem to this triangle we obtain $r_{we}$ as follows:

$$r_{we} = \sqrt{{r_w}^2 - \frac{(L_d - l_{de})^2}{4}}. \tag{9}$$

We consider the angle $\delta$ between $L_2$ and the axis $x_G$, given by the mechanical design for the effective radius $r_{ge}$ calculation:

$$r_{ge} = |r_w \cdot \sin(\rho - \delta)|. \tag{10}$$

### *3.2. Longitudinal Model*

We derive the kinematic model of the PDDB to find position variation given in the following matrix:

$$\begin{bmatrix} \dot{x} \\ \dot{y} \\ \dot{\alpha} \end{bmatrix} = \begin{bmatrix} cos(\alpha) & 0 \\ sin(\alpha) & 0 \\ 0 & 1 \end{bmatrix} \begin{bmatrix} v_d \\ \omega_w \end{bmatrix}, \tag{11}$$

where $(\dot{x}, \dot{y}$, and $\dot{\alpha})$ are the derivatives of the robot's position and the orientation; $v_d$ represents the linear velocity; and $\omega_w$ is the angular velocity.

The robot inverse Jacobian matrix describes the PDDB rollers' surface velocities that can be established as:

$$\begin{bmatrix} \omega_l \\ \omega_r \end{bmatrix} = \begin{bmatrix} \frac{1}{r_{we}} & -\frac{l_{de}}{2 \cdot r_{we}} \\ \frac{1}{r_{we}} & \frac{l_{de}}{2 \cdot r_{we}} \end{bmatrix} \begin{bmatrix} v_d \\ w_w \end{bmatrix}, \tag{12}$$

where $\omega_r$ and $\omega_l$ represent the right and left rolling velocities. The linear velocity of the PDDB center is used. The grasp rolling velocity $\omega_g$ is determined as:

$$\omega_g = \frac{\omega_r + \omega_l}{2}. \tag{13}$$

### 3.3. Heading Error

The robot's orientation influences the grasping during locomotion. The optimal heading is considered when the PDDB centerline is aligned with the longitudinal limb axis, so the orientation angle $\alpha$ is null, as shown in Figure 3. Adjusting the PDDB rollers' velocities allows it to reach a centered orientation while the decentered orientation increases $\alpha$, causing the pivot point to move away from the centerline. Therefore, $\alpha$ can be considered as a heading error for controlling orientation.

The estimation of the heading $\hat{\alpha}$ with respect to the limb longitudinal axis (Heading Estimation block in Figure 5) can be obtained from external sensors (e.g., sets of short-distance laser range-sensors) or by numerically integrating the Cartesian angular velocity ($\omega_a$) of the robot considering a known initial state:

$$\begin{bmatrix} v_d \\ \omega_a \end{bmatrix} = r_{we} \begin{bmatrix} \frac{1}{2} & \frac{1}{2} \\ \frac{1}{l_{de}} & \frac{1}{l_{de}} \end{bmatrix} \begin{bmatrix} \omega_l \\ \omega_r \end{bmatrix}. \tag{14}$$

This approach is affected by the deviation caused by cumulative inaccuracies in odometer measurements. However, as will be described in Section 4, additional performance information of the system ($\hat{\gamma}$) can be used to compensate for the estimation drift.

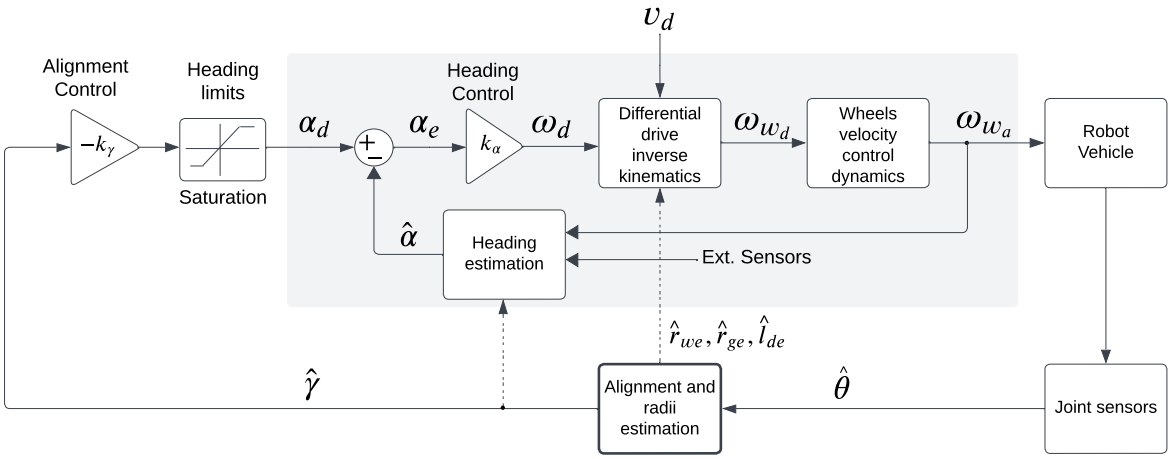


**Figure 5.** The control system block diagram shows the cascade control strategy. Alignment control (outer loop) uses proportional action for grasping stability, and heading control (inner loop) adjusts the trajectory by proportional control of PDDB rollers' velocities.

## 4. Control Strategy

In this section, the control strategy is formulated based on several assumptions. The pivot mechanism is assumed to be rigid and symmetric with respect to the longitudinal axis of the limb. Furthermore, the model considers a perpendicular contact point of the roller with the skin, so traction and adherence are guaranteed. Additionally, the analysis presupposes the absence of slippage. Moreover, we assume the robot's path is continuous and does not constitute a control objective. Also, the forward velocity is constant. Dynamics analysis and the influence of gravity are excluded.

The proposed cascade control scheme is shown in Figure 5, with the alignment control represented externally and the heading control internally (within the shaded box). The

variables to control are $\gamma$ and $\alpha$. The aim of the control system is to minimize the $\hat{\gamma}$ error estimation and to ensure that the robot motion remains parallel to the limb (i.e., $\hat{\alpha}$ is null).

The subindexes $a$, $d$, and $e$ (e.g., $\omega_a$) are used to represent their respective relationships with the actual $a$, the desired $d$, and the error $e$ value.

### *4.1. Central Alignment Control*

The external control follows a proportional control law $-k_\gamma \hat{\gamma}$, outputting a desired heading $\alpha_d$ that is limited to maintain the grasp stability. The controller input $\hat{\gamma}$ is derived from the central alignment and radius error estimation block, which receives information from the joint sensors $\theta_1$ and $\theta_2$.

Additionally, note that the alignment and radius error estimation block computes the effective differential wheel distance $l_{de}$, radii $r_{we}$, and $r_{ge}$ based on Equations (8), (9), and (10), respectively. These data are important for calculating inverse kinematics, which determines $\omega_r$, $\omega_l$, and $\omega_g$ as shown in Equations (12) and (13). The heading limits saturate the central alignment control to ensure the robot stays centered within $\pm\alpha_{d_{max}}$.

### *4.2. Heading Control*

The second loop controls the heading error $(\alpha_d - \hat{\alpha})$ with a proportional control law with gain $k_\alpha$. The estimated orientation error $\hat{\alpha}$ is computed from roller odometry. The robot follows the trajectory varying the velocity of the PDDB's rollers; these are deduced by the differential drive inverse kinematics with $v_d$ and $\omega_d$ as input references. The output is the desired velocity of each roller, given as $[\omega_{w_d}] = [\omega_{r_d}, \omega_{l_d}, \omega_{g_d}]^T$. As mentioned in Section 3.3, the drift in the odometric estimation of the heading has an effect on the overall control system. As the external control loop has a proportional control, the system error would grow proportional to the $\hat{\alpha}$ drift. To avoid this, an additional term can be added to the heading estimation (15) that compensates for the estimation error based on the integral of the error $\hat{\gamma}$ with a gain $k_i$:

$$\hat{\alpha} = \int_0^t \omega_a dt + k_i \int_0^t \hat{\gamma} dt \tag{15}$$

### *4.3. Velocity Control*

This is an additional velocity control that provides independent control of each roller of the PDDB. A PID is implemented to control the velocity of the wheels. The feedback for this control is obtained from the encoders. A first-order system has been implemented to create a model that simulates a simplified representation of the real system. The first-order transfer function simulates the loop response of the control system, with a time constant of $\tau = 65$ ms. Also, the actual velocities can be obtained as $[\omega_{w_a}] = [\omega_{r_a}, \omega_{l_a}, \omega_{g_a}]^T$. The robot vehicle block determines the global position of the robot, integrating roller velocities from Equation (11).

### *4.4. Stability Analysis*

This study aims to ensure the robot is stable while moving along a straight path along the cylinder's longitudinal axis. We propose the control's input $v = -k_\gamma \cdot \gamma$ for the grasp stability analysis. The time derivative of $\dot{v}$ and $\dot{\hat{\gamma}}$ are established at Equations (16) and (17):

$$\dot{v} = k_\gamma \cdot \dot{\gamma}, \tag{16}$$

$$\dot{\gamma} = -\dot{\theta}_1 - \dot{\beta}, \tag{17}$$

involving the temporal variation of $\theta_1$ and $\beta$, where $\beta$ is the angle between $L_1$ and $L_g$ and is derived in Equation (1). Distributing the $k_\gamma$ term, we obtain $\dot{v} = k_\gamma \cdot (-\dot{\theta}_1 - \dot{\beta})$. Solving $\dot{\beta}$ in terms of $\dot{v}$ and $\dot{\theta}_1$, the expression is:

$$\dot{\beta} = -\frac{1}{k_\gamma} \cdot \dot{v} - \dot{\theta}_1. \tag{18}$$

To guarantee the convergence and stability, a Lyapunov function candidate $V$ is chosen as $V(\theta_1, \beta) = \frac{1}{2}(\theta_1^2 + \beta^2)$, which is continuous, and positive definite $V > 0$. Computing the time derivative $\dot{V}$ we have:

$$\dot{V} = \dot{\theta}_1 \cdot \theta_1 + \dot{\beta} \cdot \beta. \tag{19}$$

If we substitute $\dot{\theta}_1$ from model Equation (18), then:

$$\dot{V} = \dot{\theta}_1 \cdot \theta_1 + \beta\left(-\frac{1}{k_\gamma} \cdot \dot{v} - \theta_1\right) \tag{20}$$

This shows that the term $-\beta \cdot \frac{1}{k_\gamma} \cdot \dot{v}$ is semidefinite negative. This guarantees the stable behavior in the system. Additionally, achieving global asymptotic stabilization of $\hat{\gamma} = 0$, indicating that the system converges to a stable equilibrium point.

## 5. Experiments and Results

This section presents the simulation of the kinematic system outlined in Section 3 and assesses the control system for alignment and heading described in Section 4, including the definition of a boundary proximity condition. Also, experimental results of locomotion are included. The results highlight the robot's capabilities to control the direction of the PDDB and maintain stable limb grasp alignment.

### *5.1. Simulation Parameters*

The simulation experiments were developed using MATLAB by Mathworks (Natick, MA, USA) running on a 2.3 GHz 8-Core (Core i9) by Intel Corp. (Santa Clara, CA, USA) with 16 GB 2667 MHz DDR4 memory. For the simulations, we used parameters considered relevant for an on-arm robot: $r_w = 20$ mm, $L_d = 42$ mm, and $\gamma = 90/\pi$rad, with $r_c$ radii ranging from 28 mm to 50 mm. When simulating the joint sensors $\theta_1$ and $\theta_2$, we started from the position $P_g$ and determined $L_g$ by applying the concept of the distance between $O$ and $G$. Next, we derived $\theta_2$ according to the law of cosines. In case $L_1$ and $L_2$ are equal, the equation can be simplified as: $\theta_2 = \cos^{-1}\left(({L_g}^2 - 2 \cdot {L_1}^2)/(-2 \cdot {L_1}^2)\right)$. Subsequently, $\beta$ is found using the sum of the interior angles of the isosceles triangle $P_1P_2G$, given by $\beta = (\pi - \theta_2)/2$, based on Equation (2) of $\gamma$ and with $\beta$ information, we determine $\theta_1$, that can be estimated as: $\theta_1 = \frac{\pi}{2} - (\gamma + \beta)$.

### *5.2. Boundary Proximity Condition*

A cylinder with varying radii represents the outer surface of the limb. A boundary proximity condition has been implemented to ensure that the simulated robot does not pass through the cylinder. The condition detects when the limb contacts the spring joint, requiring a distance $L_{bc}$ between the limb border and point $P_2$ on the spring joint to maintain this restriction:

$$L_{bc} = \sqrt{{L_1}^2 - \frac{3 \cdot r^2 - \frac{{L_d}^2}{4} + 2 \cdot r \cdot \sqrt{r^2 - \frac{{L_d}^2}{4}}}{4}} - r_c, \tag{21}$$

where $r = r_c + r_w$, and $L_{bc}$ defines a relationship between $r_c$, $r_w$, and $L_d$. For the sake of simplicity, Equation (21) assumes $L_1 = L_2$.

### *5.3. Simulation Results*

Simulated experiments have been performed to evaluate the performance of the cascade control, the effect of different limb sizes, and the compensation of drift in heading estimation.

#### 5.3.1. Cascade Control Performance

Figure 6 presents simulation results in robot coordinates. The initial conditions of the experiment are $v_l$ =10 mm/s, $L_d = 42$, $r_w = 20$ mm, and $L_1 = L_2 = 82.23$ mm, where an initial alignment error of the grasp wheel is corrected while the robot follows a trajectory

parallel to the longitudinal cylinder axis. The cascaded alignment and heading controls guarantee stability and locomotion on a varying radius limb. Figure 6a–c illustrate the robot's front view, $XY$ plane, at three representative moments of the simulation. Evolution of the grasping alignment error $\hat{\gamma}$, the trajectory results of the joint angle sensors are shown in Figure 6d. The findings indicate a shift in the wheels' position, resulting in a stable grasp on the limb and continuous grasping during locomotion.

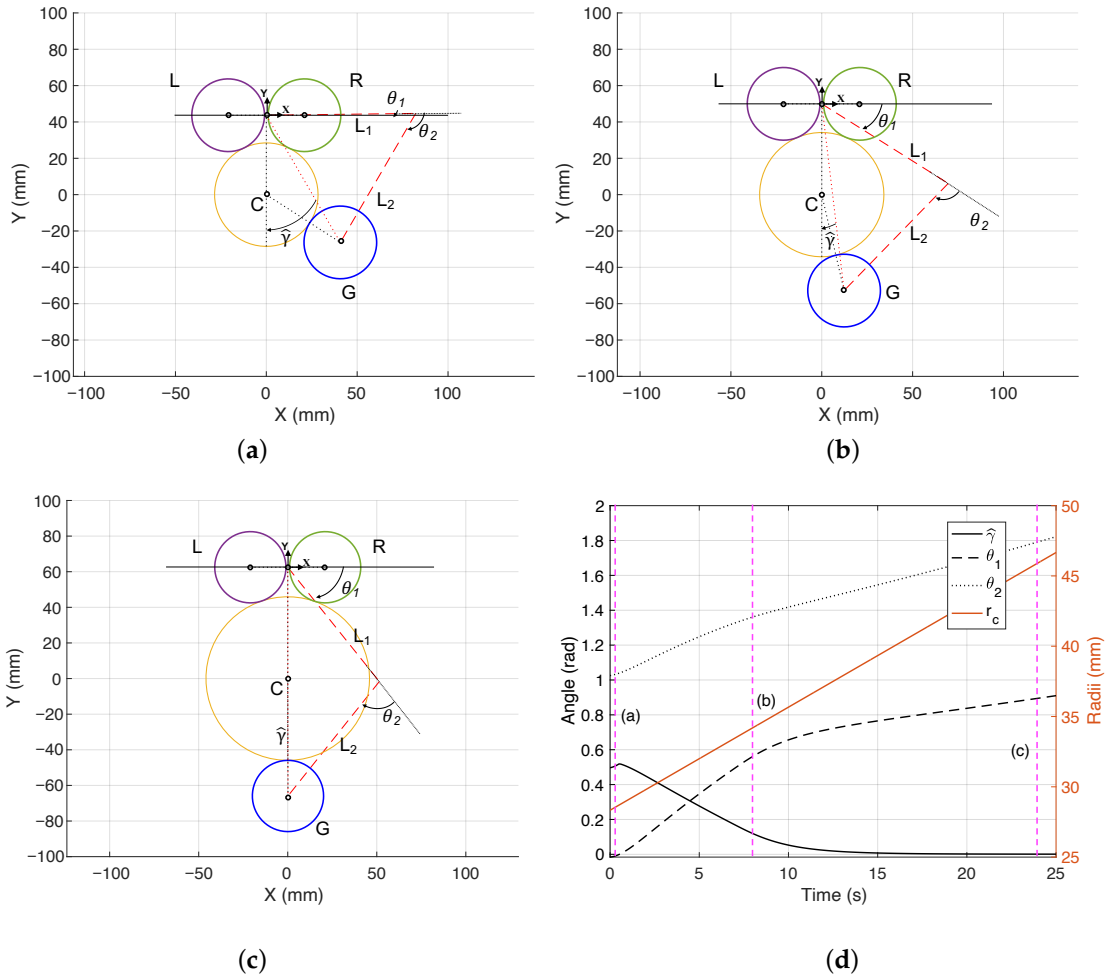


**Figure 6.** Path of the grasp roller in a variable diameter limb from the front view: (**a**) position at $t = 0.28$ s, (**b**) advancement of the grasp roller at $t = 8$ s, (**c**) at $t = 24$ s, and (**d**) evolution of $\hat{\gamma}$, $\theta_1$, $\theta_2$, and $r_c$ variation, where instants corresponding to (**a**–**c**) are highlighted by fuchsia dashed lines.

Furthermore, we have evaluated the effect of different heading limit values $\alpha_{d_{max}}$ in the cascaded control system, as shown in Figure 7. In particular, heading limits have been set for $\pm 0.08$ rad, $\pm 0.17$ rad, and $\pm 0.43$ rad. In the first case, the control system shows a slow response after reaching $\alpha_{max}$, resulting in an extended period before overcoming the condition. Conversely, the last test indicates the robot approaches $\alpha_{max}$ too quickly, causing it to move faster than required. This could be problematic, as the vehicle must control the wheel speeds differently to change direction. In all simulations, the radius was considered to vary along the trajectory.

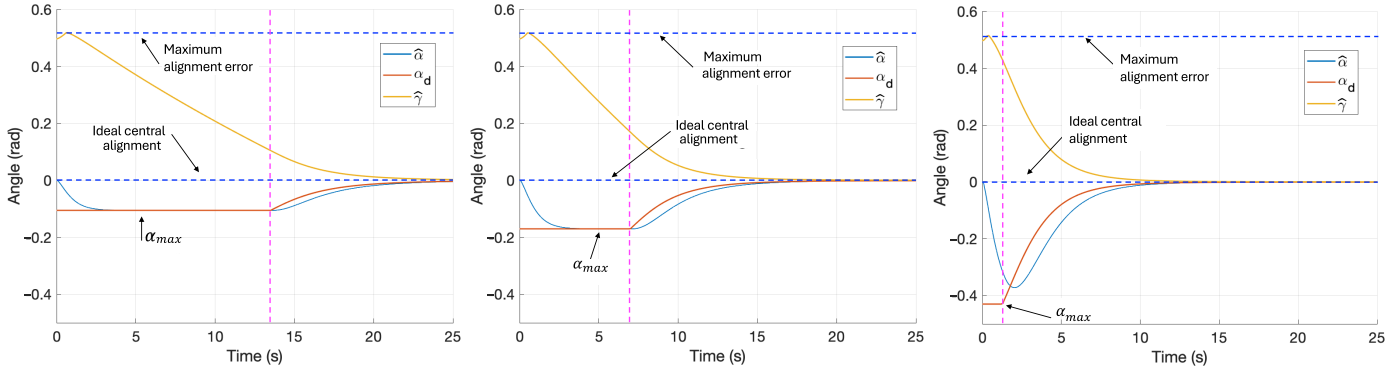


**Figure 7.** Effect of $\alpha_{max}$ in the temporal response from $\hat{\gamma}$ (with an initial value of 0.52 rad), $\hat{\alpha}$, and $\alpha_d$, in a variable diameter limb. (**a**) $\alpha_{max}$ = 0.10 rad: $\hat{\alpha}$ begins to overcome the heading condition at $t$ = 13.60 s; (**b**) $\alpha_{max}$ = 0.17 rad: $\hat{\alpha}$ overcomes the heading condition at $t$ = 6.9 s; and (**c**) $\alpha_{max}$ = 0.43rad: $\hat{\alpha}$ approaches the heading condition at $t$ = 1.25 s.

#### 5.3.2. Effect of Different Limb Sizes

Table 3 presents results for different limb sizes according to minimum ($r_{c_{min}}$) and maximum ($r_{c_{max}}$) limb radii: small (S), medium (M), and large (L), which correspond to human arm radius variations between 22 and 42 mm, 24 and 44 mm, and 28 and 50 mm, respectively, [41]. Moreover, different values for the parameter $L_d$ (40 mm, 44 mm, and 48 mm) are considered. In these experiments, the robot starts from the wrist ($r_{c_{min}}$). The table presents the resulting maximum alignment error $\gamma_{max}$, the settling time $t_{s_\gamma}$, measured as the time required for $\gamma$ to fall within = $\pm$0.05 rad, and the corresponding traveled distance in that time $d_{s_\gamma}$. Increasing $L_d$ provokes a slight reduction in $\gamma_{max}$ but has a negligible effect on settling time and distance. The major observed performance differences depend on limb size, with longer settling times for the L-sized arm.

**Table 3.** Parameters $L_d$, $r_c$, and $\gamma$ for different component sizes and configurations with $v_l$ = 10 mm/s, and $\alpha_{max}$ = 0.17 rad, starting from $r_{c_{min}}$.

| **Size** | $S_{40}$ | $S_{44}$ | $S_{48}$ | $M_{40}$ | $M_{44}$ | $M_{48}$ | $L_{40}$ | $L_{44}$ | $L_{48}$ |
|---|---|---|---|---|---|---|---|---|---|
| $L_d$ (mm) | 40.00 | 44.00 | 48.00 | 40.00 | 44.00 | 48.00 | 40.00 | 44.00 | 48.00 |
| $r_{c_{min}}$ (mm) | 22.00 | 22.00 | 22.00 | 24.00 | 24.00 | 24.00 | 28.00 | 28.00 | 28.00 |
| $r_{c_{max}}$ (mm) | 42.00 | 42.00 | 42.00 | 44.00 | 44.00 | 44.00 | 50.00 | 50.00 | 50.00 |
| $\gamma_{max}$ (rad) | 0.4608 | 0.4604 | 0.4531 | 0.4888 | 0.4833 | 0.4811 | 0.5204 | 0.5170 | 0.5153 |
| $d_{s_\gamma}$ (mm) | 78.14 | 77.14 | 77.14 | 86.04 | 86.04 | 86.04 | 99.89 | 99.89 | 98.88 |
| $t_{s_\gamma}$ (s) | 7.90 | 7.80 | 7.80 | 8.70 | 8.70 | 8.70 | 10.10 | 10.10 | 10.10 |

#### 5.3.3. Drift Compensation in Heading Estimation

As mentioned in Section 4.2, the deviation caused by cumulative inaccuracies in odometer measurements can be avoided either by using external sensors or by using the integral of the alignment error (15). In this work, no external sensors have been used, and the drift of odometric estimation is compensated by the alignment error, which in turn makes use of the proprioceptive sensors located in joints $\theta_1$ and $\theta_2$. To show the compensation capability of the heading estimation block (15), a simulation experiment has been performed by adding a ramp (0.015 deg/s), to the $\hat{\alpha}$ signal and an integral constant $k_i$ = 0.1. Additionally, an $\alpha_{max}$ = 0.17 rad and a linear velocity $v_l$ = 20 mm/s are used.

As shown in Figure 8, in steady state, the uncompensated heading $\hat{\alpha}$, unlike the compensated heading $\hat{\alpha}_i$, follows the simulated drift. The steady value of the $\hat{\alpha}_i$ is null, so the alignment error can also be null. We also believe that this approach may also compensate for the effects of non-straight limbs.

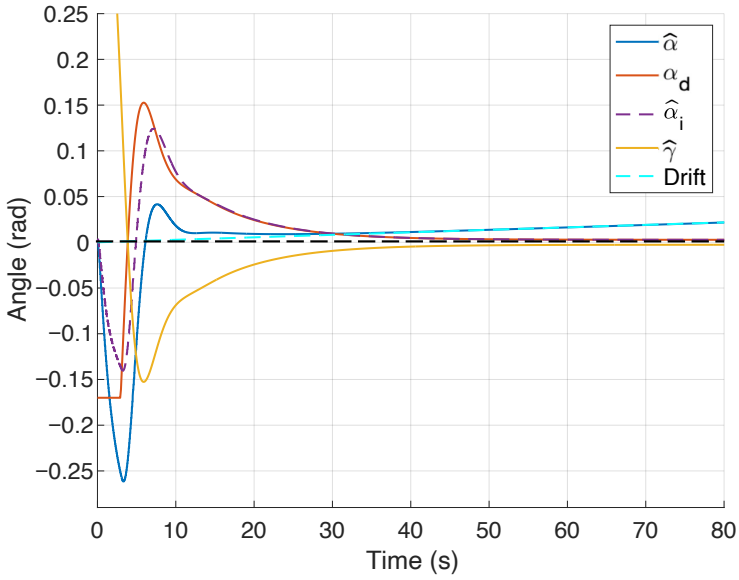


**Figure 8.** Compensation of the odometric heading estimation error using the alignment error signal with a simulated drift.

### *5.4. 3D Visualization of Robot Locomotion*

Robot locomotion visualization is shown in Figure 9, which illustrates the pivoting movement of the PDDB and the control system involved in heading adjusting. Furthermore, it shows the grasp movement along the upper arm. The simulation illustrates three positions: initial, progress, and final. Moreover, the dimensions of the limb were based on the anthropometric measurements. We establish for the wrist radius the range from 22 mm to 32 mm; for the mid-limb, between 32 mm to 44 mm; and the limb, between 42 mm to 54 mm [42]. In addition, longitudinal distances were established from the wrist to the mid-limb, with a range of 120 mm to 180 mm, and from the mid-limb to the shoulder, with a range of 165 mm to 225 mm [41]. Once the limb radius ranges were defined, we interpolated the data and conducted a fitting process, all as part of the limb modeling.

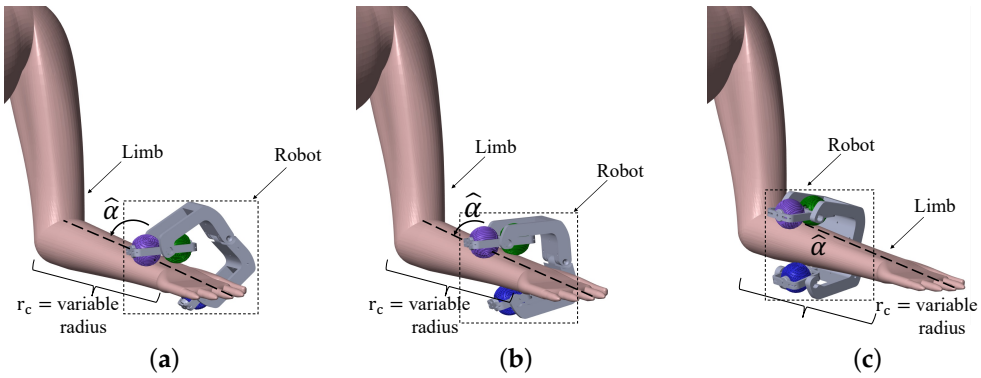


**Figure 9.** Locomotion of the virtual model along the upper limb: (**a**) initial position at $t = 0.28$ s, (**b**) advancement of the grasp wheel at $t = 8$ s, and (**c**) final position at $t = 24$ s.

### *5.5. Link Length Design*

The structure design can influence the stability of the on-limb mobile robot. Therefore, we analyze the parameters of the differential wheel distance $L_d$, roller radius $r_w$, and the limb radius, $r_c$, represented as a cylinder. We consider a range of 40 mm to 48 mm for $L_d$, and for $r_w$, the range is between 16 mm and 24 mm. With this data, we computed the maximum $r_{c_{max}}$. The results are presented in Table 4, in which we compare how changes in $L_d$ and $r_w$ affect the maximum limb radius $r_{c_{max}}$. As $L_d$ rises, $r_{c_{max}}$ decreases. Increasing $L_d$ could improve stability but also would affect the robot's change direction as well as the

navigation on the upper limb and adaptation to changes in limb dimensions. Furthermore, we establish a design criterion, $L_d < 2 \cdot r_w$, indicating that the differential wheel distance should be less than twice the wheel radius. This prevents oversizing issues that may lead to undesirable wheel contact.

**Table 4.** Maximum limb radius $r_{c_{\max.}}$ for $L_d$ and $r_w$ design parameters.

| $L_d$ (mm) | $r_w$ (mm) | $r_{c_{\max}}$ (mm) |
|---|---|---|
| 40.00 | 16.00 | 50.48 |
| 40.00 | 20.00 | 48.10 |
| 40.00 | 24.00 | 45.78 |
| 44.00 | 16.00 | 50.61 |
| 44.00 | 20.00 | 48.35 |
| 44.00 | 24.00 | 45.92 |
| 48.00 | 16.00 | 50.92 |
| 48.00 | 20.00 | 48.53 |
| 48.00 | 24.00 | 46.18 |

### *5.6. Developed Prototype*

We constructed a prototype to verify the kinematic model's design and simulation results. The PDDB has dimensions of $W_l = 85.52$ mm and $L_b = 76$ mm, as shown in Figure 10. Link length parameters are $L_1 = L_2 = 82.23$ mm, roller radii are $r_w = 20$ mm, $L_d = 48$ mm, and $\delta = 0.54$ rad. The robot includes three small in-wheel DC motors, each with encoders by Pololu Robotics and Electronics (Las Vegas, NV, USA). These motors are velocity-controlled independently, and the motor shaft connects to the center of each wheel. Also, two rotary potentiometers with good performance in robotic grippers [43], muRata A01346 by Murata Manufacturing Co., Ltd. (Nagaokakyo-shi, Japan), are affixed to Link 1 to measure the pivoting and spring joint angles (i.e., $\theta_1$ and $\theta_2$). The wheels feature a surface pattern that hlserves to verify visually advance and the PDDB directional changes. The PDDB, links, the spherical wheels, and the spring joint brackets were 3D printed in polylactide (PLA) material. All in all, the robot weighs 250 g, including the three wheel-motor sets (26 g each). Table 5 shows the weight of each component of the robot. A Mega2560 microcontroller by Arduino (Chiasso, Switzerland) processes the angle sensor data and controls the three in-wheel motors for velocity. In the experimental prototype, this microcontroller has not been integrated on-board.

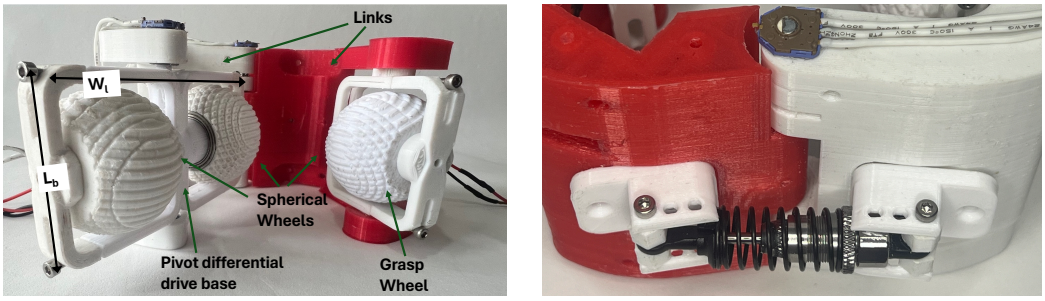


(**a**) (**b**)

**Figure 10.** Prototype of the on-limb mobile robot: (**a**) general view; (**b**) detail of the spring joint with rotatory sensor.

**Table 5.** Parts and their weights.

| Parts | Weight (g) |
|---|---|
| 3 Wheels with motors | 78 |
| Links $L_1$ and $L_2$ | 124 |
| PDDB without motors | 16 |
| Grasp wheel base | 9 |
| Spring | 9 |
| 2 Brackets | 4 |
| Mechanical and fastening components | 10 |
| Total | 250 |

For the passive joint mechanism, we used an aluminum alloy shock absorber designed for radio-controlled cars with an elastic constant of 60 N/m [44]. The rest, pre-load, and maximum lengths of the spring are 16 mm, 44.7 mm, and 60 mm, respectively. We empirically found that this spring offered a good balance between grasping force and comfort. Moreover, both links have three spring anchor points allowing the tension to be adjusted for different users (see Figure 10).

The experimental simulation results depict $\gamma$ and $\alpha$ values across velocities ranging from $v = 5\,\text{mm/s}$ to $v = 25\,\text{mm/s}$, utilizing the mechanical parameters: $r_w = 20$ mm, $L_d = 48$ mm, $L_1 = L_2 = 82.23$ mm, and $\alpha_{max} = 0.17$ rad. These results are illustrated in Figure 11.

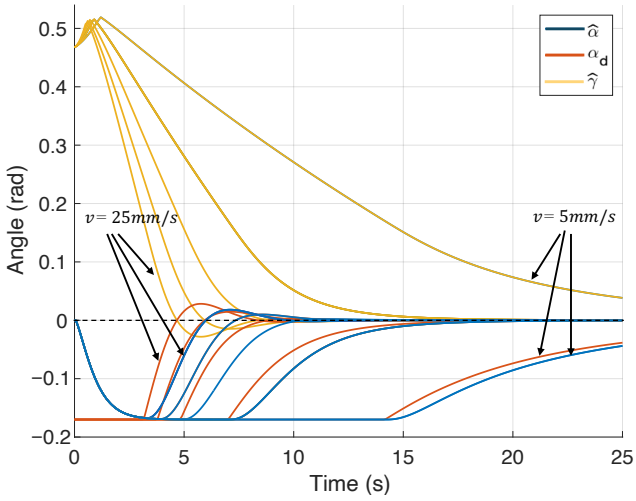


**Figure 11.** Temporal evolution of $\gamma$ and $\alpha$ for velocities from $v = 5$ mm/s to $v = 25$ mm/s.

The on-limb mobile robot locomotion tests (see Figure 12) were teleoperated. We used virtual sensors based on the upper limb dimensions, thus allowing the robot to track the movements. The robot considers variations in limb sizes and dimensions. The spring joint has three positions that increase the opening range and reduce friction force. Results show that the robot moves over the limb. Also, spherical rollers offer advantages such as a circular contact area, which eliminates pressure points and thus reduces user discomfort.

Even if no clinical experiments have been performed, voluntary users in preliminary lab tests described their sensations as comfortable and natural, noting the device's smooth adaptation to the limb's anatomical shape, the absence of annoying noises, and the perception of fluid, non-intrusive movements.

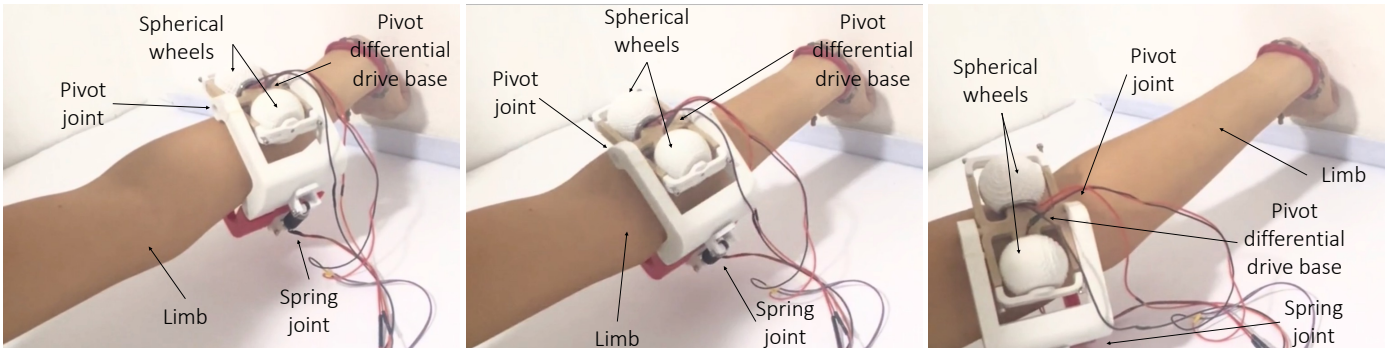


(**a**) (**b**) (**c**)

**Figure 12.** Temporal progression of locomotion on a human upper limb: (**a**) initial position, (**b**) intermediate position, and (**c**) final position.

## 6. Conclusions

We have presented a novel on-limb mobile robot mechanism adaptable to human limb sizes. Concerning the mechanical design, the combination of the spring joint, the free pivoting mechanism, and the spherical wheels provides a solution that guarantees continuous three-wheel contact with the limb. Also, the open mechanism allows for the robot to be easily put on or removed at any point on the limb without slipping the robot over the hand or foot. While alternative solutions, such as a closed mechanisms or bracelet, offer intrinsic grasping stability, achieving mechanical stability poses a challenge in open mechanisms. Implementing a double cascade control system enables the robot to achieve grasping stability while enhancing maneuverability through differential drive steering. Moreover, the controller includes drift compensation in odometric heading estimation.

The simulations have demonstrated the effectiveness of the controller to maintain heading and central alignment. Furthermore, an on-limb robot prototype has been built to test its applicability to human arms.

Nevertheless, further work is required for practical application, including clinical experiments to evaluate user experience and comfort during extended use. Additionally, there is potential to optimize materials and robot design to reduce weight and facilitate the integration of electronics for untethered operation. Moreover, the estimation of heading error has been performed using odometry. A more accurate estimation of this value is related to the complex problem of on-body robot localization, which requires additional proprioceptive and/or exteroceptive sensors. Moreover, analyzing gravity and wheel–skin tissue interactions with terramechanics principles, involving wheel surface materials and human tissue modeling, is an open research area for on-limb robots.

**Author Contributions:** Conceptualization, L.M.T.-S.-C. and J.M.G.-d.-G.; methodology, L.M.T.-S.-C., J.M.G.-d.-G. and A.M.; software, L.M.T.-S.-C. and J.M.G.-d.-G.; validation, L.M.T.-S.-C. and J.M.G.-d.-G.; formal analysis, L.M.T.-S.-C., A.M. and J.M.G.-d.-G.; investigation, L.M.T.-S.-C. and J.M.G.-d.-G.; writing—original draft, L.M.T.-S.-C., A.M. and J.M.G.-d.-G.; writing—review and editing, L.M.T.-S.-C., A.M. and J.M.G.-d.-G.; visualization, L.M.T.-S.-C.; supervision, A.M. and J.M.G.-d.-G.; project administration, J.M.G.-d.-G.; funding acquisition, J.M.G.-d.-G. All authors have read and agreed to the published version of the manuscript.

**Funding:** This work has been funded by the "Plan Nacional de Investigacion de España" under a project with code PID2021-127221OB-I00. This publication has also been partially funded by the Universidad de Málaga.

**Institutional Review Board Statement:** The study was conducted in accordance with the Declaration of Helsinki, and the protocol was approved by the Ethics Committee of the University of Málaga (CEUMA) with reference 7-2023-H, 13 June 2023.

**Informed Consent Statement:** Not applicable.

**Data Availability Statement:** All data included in this study are available upon request by contact with the corresponding author.

**Acknowledgments:** The first author has received a research stay grant by AUIP—Programa Iberoamericano de Formación Doctoral en el área de las Ingenierías y las Ciencias Técnicas.

**Conflicts of Interest:** The authors declare no conflicts of interest.

## Abbreviations

The following abbreviations are used in this manuscript:

| | |
|---|---|
| DOF | Degrees of freedom |
| PDDB | Pivoting differential drive base |

## References

1. Park, S.; Jayaraman, S. Wearables: Fundamentals, advancements, and a roadmap for the future. In *Wearable Sensors*, 2nd ed.; Academic Press: Oxford, UK, 2021; Chapter 1, pp. 3–27. [CrossRef]
2. Shtarbanov, A.; Zhu, M.; Colonnese, N.; Hajiagha Memar, A. SleeveIO: Modular and Reconfigurable Platform for Multimodal Wearable Haptic Feedback Interactions. In Proceedings of the Annual ACM Symposium on User Interface Software and Technology, San Francisco, CA, USA, 29 October–1 November 2023. [CrossRef]
3. Minaoglou, P.; Efkolidis, N.; Manavis, A.; Kyratsis, P. A Review on Wearable Product Design and Applications. *Machines* **2024**, *12*, 62. [CrossRef]
4. Pons, J. *Wearable Robots: Biomechatronic Exoskeletons*; John Wiley and Sons: Hoboken, NJ, USA, 2008. [CrossRef]
5. Pitzalis, R.F.; Park, D.; Caldwell, D.G.; Berselli, G.; Ortiz, J. State of the Art in Wearable Wrist Exoskeletons Part II: A Review of Commercial and Research Devices. *Machines* **2024**, *12*, 21. [CrossRef]
6. Chinello, F.; Malvezzi, M.; Pacchierotti, C.; Prattichizzo, D. Design and development of a 3RRS wearable fingertip cutaneous device. In Proceedings of the IEEE International Conference on Advanced Intelligent Mechatronics, Busan, Republic of Korea, 7–11 July 2015; pp. 293–298. [CrossRef]
7. Mete, M.; Paik, J. Closed-Loop Position Control of a Self-Sensing 3-DoF Origami Module With Pneumatic Actuators. *IEEE Robot. Autom. Lett.* **2021**, *6*, 8213–8220. [CrossRef]
8. Tong, Y.; Liu, J. Review of Research and Development of Supernumerary Robotic Limbs. *IEEE CAA J. Autom. Sin.* **2021**, *8*, 929–952. [CrossRef]
9. Rahman, A.; Azim, M.A.R.; Heo, S. Take My Hand: Automated Hand-Based Spatial Guidance for the Visually Impaired. In Proceedings of the Conference on Human Factors in Computing Systems, Hamburg, Germany, 23–28 April 2023. [CrossRef]
10. Dementyev, A. Dynamic Wearable Technology: Designing and Deploying Small Climbing Robots for Sensing and Actuation on the Human Body. Ph.D. Thesis, Massachusetts Institute of Technology, Cambridge, MA, USA, 2019.
11. Dementyev, A.; Jitosho, R.; Paradiso, J.A. Mechanical imaging of soft tissues with miniature climbing robots. *IEEE Trans. Biomed. Eng.* **2021**, *68*, 3142–3150. [CrossRef] [PubMed]
12. Wu, X.; Liu, J.; Zhou, Y.; Lv, Q.; Hu, C. Movement Control and Attitude Adjustment of Climbing Robot on Flexible Surfaces. *IEEE Trans. Ind. Electron.* **2018**, *65*, 2618–2628. [CrossRef]
13. Dobbelstein, D.; Stemasov, E.; Besserer, D.; Stenske, I.; Rukzio, E. Movelet: A self-actuated movable bracelet for positional haptic feedback on the user's forearm. In Proceedings of the ACM International Symposium on Wearable Computers, Singapore, 8–12 October 2018. [CrossRef]
14. Sathya, A.; Li, J.; Rahman, T.; Gao, G.; Peng, H. Calico: Relocatable On-cloth Wearables with Fast, Reliable, and Precise Locomotion. *Proc. ACM Interact. Mob. Wearable Ubiquitous Technol.* **2022**, *6*, 1–32. [CrossRef]
15. Kao, H.L.; Ajilo, D.; Anilionyte, O.; Dementyev, A.; Choi, I.; Follmer, S.; Schmandt, C. Exploring interactions and perceptions of kinetic wearables. In Proceedings of the Conference on Designing Interactive Systems, Edinburgh, UK, 10–14 June 2017; pp. 391–396. [CrossRef]
16. Kimura, K.; Tanaka, F. Development of a Wearable Robot that Moves on the User's Arm to Provide Calming Interactions. In Proceedings of the ACM/IEEE International Conference on Human-Robot Interaction, Stockholm, Sweden, 13–16 March 2023; pp. 311–313. [CrossRef]
17. Liu, F.; Patil, V.; Erickson, Z.; Temel, Z. Characterization of a Meso-Scale Wearable Robot for Bathing Assistance. In Proceedings of the IEEE International Conference on Robotics and Biomimetics (ROBIO), Jinghong, China, 5–9 December 2022; pp. 2146–2152. [CrossRef]
18. Sikdar, S.; Rahman, M.H.; Siddaiah, A.; Menezes, P.L. Gecko-Inspired Adhesive Mechanisms and Adhesives for Robots—A Review. *Robotics* **2022**, *11*, 143. [CrossRef]
19. Fang, G.; Cheng, J. Advances in Climbing Robots for Vertical Structures in the Past Decade: A Review. *Biomimetics* **2023**, *8*, 47. [CrossRef]
20. Jamšek, M.; Sajko, G.; Krpan, J.; Babič, J. Design and Control of a Climbing Robot for Autonomous Vertical Gardening. *Machines* **2024**, *12*, 141. [CrossRef]

21. Dementyev, A.; Hernandez, J.; Choi, I.; Follmer, S.; Paradiso, J. Epidermal Robots: Wearable Sensors that Climb on the Skin. *Proc. Acm Interact. Mob. Wearable Ubiquitous Technol.* **2018**, *2*, 1–22. [CrossRef]
22. Liu, Y.; Wu, X.; Qian, H.; Zheng, D.; Sun, J.; Xu, Y. System and design of clothbot: A robot for flexible clothes climbing. In Proceedings of the IEEE International Conference on Robotics and Automation, St. Paul, MN, USA, 14–18 May 2012; pp. 1200–1205. [CrossRef]
23. Chen, G.; Liu, Y.; Fu, R.; Sun, J.; Wu, X.; Xu, Y. Rubbot: Rubbing on flexible loose surfaces. In Proceedings of the IEEE/RSJ International Conference on Intelligent Robots and Systems, Tokyo, Japan, 3–7 November 2013; pp. 2303–2308. [CrossRef]
24. Dementyev, A.; Kao, C.H.L.; Choi, I.; Ajilo, D.; Xu, M.; Paradiso, J.; Schmandt, C.; Follmer, S. Rovables: Miniature On-Body Robots as Mobile Wearables. In Proceedings of the 29th Annual Symposium on User Interface Software and Technology, Tokyo, Japan, 16–19 October 2016; pp. 111–120. [CrossRef]
25. Birkmeyer, P.; Gillies, A.G.; Fearing, R.S. CLASH: Climbing vertical loose cloth. In Proceedings of the IEEE/RSJ International Conference on Intelligent Robots and Systems, San Francisco, CA, USA, 25–30 September 2011; pp. 5087–5093. [CrossRef]
26. Saga, T.; Munekata, N.; Ono, T. Daily support robots that move on me. In Proceedings of the SIGGRAPH Asia 2014 Emerging Technologies, Singapore, 28 November–1 December 2014; pp. 1–3. [CrossRef]
27. Kim, J.H.H.; Patil, S.D.; Matson, S.; Conroy, M.; Kao, C.H.L. KnitSkin: Machine-Knitted Scaled Skin for Locomotion. In Proceedings of the Conference on Human Factors in Computing Systems, Orleans, LA, USA, 29 April–5 May 2022. [CrossRef]
28. Liu, J.H.; Padrigalan, K.E. The kinematic analysis of a wind turbine climbing robot mechanism. *Appl. Sci.* **2022**, *12*, 1210. [CrossRef]
29. Shah, D.; Dave, J.; Majithiya, A.; Patel, Y. Conceptual design and analysis of pipe climbing robot. *J. Phys. Conf. Ser.* **2021**, *2115*, 012004. [CrossRef]
30. Li, J.; Huang, F.; Tu, C.; Tian, M.; Wang, X. Elastic Obstacle-Surmounting Pipeline-Climbing Robot with Composite Wheels. *Machines* **2022**, *10*, 874. [CrossRef]
31. Wang, Z.; Wang, Y.; Zhang, B. Development and Experiment of Clamp Type Submarine Cable Inspection Robot. *Machines* **2023**, *11*, 627. [CrossRef]
32. Zheng, Z.; Zhang, W.; Fu, X.; Hazken, S.; Hu, X.; Chen, H.; Luo, J.; Ding, N. CCRobot-IV: An obstacle-free split-type quad-ducted propeller-driven bridge stay cable-climbing robot. *IEEE Robot. Autom. Lett.* **2021**, *7*, 11751–11758. [CrossRef]
33. Wan, J.; Sun, L.; Du, T. Design and applications of soft actuators based on Digital Light Processing (DLP) 3D printing. *IEEE Access* **2023**, *11*, 86227–86242. [CrossRef]
34. Mendoza, N.; Haghshenas-Jaryani, M. Combined Soft Grasping and Crawling Locomotor Robot for Exterior Navigation of Tubular Structures. *Machines* **2024**, *12*, 157. [CrossRef]
35. Xie, D.; Liu, J.; Kang, R.; Zuo, S. Fully 3D-printed modular pipe-climbing robot. *IEEE Robot. Autom. Lett.* **2020**, *6*, 462–469. [CrossRef]
36. Yuan, S.; Shao, L.; Yako, C.L.; Gruebele, A.; Salisbury, J.K. Design and control of roller grasper V2 for in-hand manipulation. In Proceedings of the 2020 IEEE/RSJ International Conference on Intelligent Robots and Systems (IROS), Las Vegas, NV, USA, 25–29 October 2020; pp. 9151–9158. [CrossRef]
37. Backus, S.B.; Dollar, A.M. An Adaptive Three-Fingered Prismatic Gripper with Passive Rotational Joints. *IEEE Robot. Autom. Lett.* **2016**, *1*, 668–675. [CrossRef]
38. Tafrishi, S.A.; Svinin, M.; Yamamoto, M.; Hirata, Y. A geometric motion planning for a spin-rolling sphere on a plane. *Appl. Math. Model.* **2023**, *121*, 542–561. [CrossRef]
39. Rimon, E.; Burdick, J. Towards planning with force constraints: On the mobility of bodies in contact. In Proceedings of the 1993 Proceedings IEEE International Conference on Robotics and Automation, Atlanta, GA, USA, 2–6 May 1993; Volume 1, pp. 994–1000. [CrossRef]
40. Poonwattanachai, K.; Niparnan, N.; Sudsang, A. Computation of Three-Finger Grasping Plane. In Proceedings of the 2018 22nd International Computer Science and Engineering Conference (ICSEC), Chiang Mai, Thailand, 21–24 November 2018; pp. 1–5. [CrossRef]
41. Schünke, M.; Schulte, E.; Schumacher, U.; Voll, M.; Wesker, K. *LernAtlas der Anatomie*; 2022. Available online: http://www.ciando.com/img/books/extract/3132420840_lp.pdf (accessed on 1 July 2024).
42. Preedy, V.R. *Handbook of Anthropometry: Physical Measures of Human Form in Health and Disease*; Springer Science & Business Media: Berlin/Heidelberg, Germany, 2012.
43. Pastor, F.; Lin-Yang, D.H.; Gómez-de Gabriel, J.M.; García-Cerezo, A.J. Dataset with Tactile and Kinesthetic Information from a Human Forearm and Its Application to Deep Learning. *Sensors* **2022**, *22*, 8752. [CrossRef] [PubMed]
44. Ruiz-Ruiz, F.J.; Urdiales, C.; Gómez-de Gabriel, J.M. Estimation of the Interaction Forces in a Compliant pHRI Gripper. *Machines* **2022**, *10*, 1128. [CrossRef]